ADVANCED ENERGY MATERIALS
www.advenergymat.de

Electron-Selective Naphthalimide-Based Monolayers for Tuned Energy Level Alignment in Halide Perovskite Solar Cells

Parnian Ferdowsi, Euimin Lee, Gyujin Jang, Jin Su Park, Donghyun Lee, Sumit Kumar Sharma, Waygen Thor, Jong-Woon Ha, Han-Hee Cho,* Jun-Ho Yum,* and Kevin Sivula**

Charge-selective contacts critically influence carrier dynamics and overall performance in halide perovskite solar cells (PSCs). Self-assembled monolayers (SAMs) have emerged as a powerful strategy for precise interfacial engineering, enabling tailored energy level alignment and interfacial interactions to enhance charge extraction. Despite their promise, clear structure–function relationships for SAMs—particularly as electron-selective contacts (ESCs)—remain poorly developed. Here, a series of naphthalimide (NI)-based SAMs functionalized with cyano, bromo, or methoxy groups and varying alkyl linker lengths are systematically evaluated as ESCs in n-i-p PSCs. Devices incorporating these SAMs exhibit power conversion efficiencies (PCEs) ranging from 5.8% to 20.6%, depending on molecular structure. The highest PCE is achieved using a SAM with a strongly electron-withdrawing cyano group and a short ethyl linker, attributed to deep LUMO alignment and efficient charge transport at the interface. In contrast, SAMs with longer linkers or higher energy levels yield inferior performance. These results reveal critical design principles for high-performance SAM-based ESCs and establish a new PCE benchmark for PSCs employing standalone SAMs, without auxiliary metal oxide layers. Overall, this work underscores the potential of molecularly engineered SAMs to enable scalable, efficient, and commercially viable perovskite photovoltaics through optimized interfacial control.

1. Introduction

Halide perovskite solar cells (PSCs) have gained significant attention due to their rapid advancements, with certified power conversion efficiencies (PCE) reaching up to 26.7%, making them comparable to silicon solar cells.[1,2] The remarkable optoelectronic properties of halide perovskites, including tunable bandgaps, large absorption coefficients, long carrier lifetimes, low exciton binding energies, and ease of fabrication, have been key factors behind this progress, and have positioned PSCs as one of the leading technologies in next-generation thin-film photovoltaics.[3–9] However, beyond the inherent properties of the perovskite materials, the multilayered device architecture must be carefully engineered to ensure efficient charge extraction as the overall device performance is strongly influenced by unfavorable recombination of accumulated charges at the interfaces. Thus, selective charge

P. Ferdowsi, J. S. Park, S. K. Sharma, W. Thor, J.-H. Yum, K. Sivula
Laboratory for Molecular Engineering of Optoelectronic Nanomaterials
Institut des Sciences et Ingénierie Chimiques
Ecole Polytechnique Fédérale de Lausanne (EPFL)
Lausanne 1015, Switzerland
E-mail: junho.yum@epfl.ch; kevin.sivula@epfl.ch

E. Lee, D. Lee, H.-H. Cho
Department of Materials Science and Engineering
Ulsan National Institute of Science and Technology (UNIST)
Ulsan 44919, Republic of Korea
E-mail: hhcho@unist.ac.kr

The ORCID identification number(s) for the author(s) of this article can be found under https://doi.org/10.1002/aenm.202502789

DOI: 10.1002/aenm.202502789

H.-H. Cho
Graduate School of Carbon Neutrality
Ulsan National Institute of Science and Technology (UNIST)
Ulsan 44919, Republic of Korea

G. Jang
Photoenergy Research Center
Korea Research Institute of Chemical Technology (KRICT)
Daejeon 34114, Republic of Korea

J.-W. Ha
Department of Materials Engineering and Convergence Technology
Gyeongsang National University
Jinju 52828, Republic of Korea
E-mail: hajw@gnu.ac.kr

extraction layers for both photogenerated holes and electrons play a crucial role by enabling directed charge transport while suppressing recombination losses.[1,10–12]

For high-performance n–i–p devices, charge transporting layers, such as tin oxide (SnO_2) for the electron transporting layer (ETL) and spiro-OMeTAD for the hole transporting layer (HTL), are commonly employed.[13–15] Similarly, for p–i–n architectures, poly(triaryl)amines and C_{60} fullerene-based derivatives are frequently used as the HTL and ETL, respectively. Despite the impressive performance of PSCs, these charge-transporting layers face several limitations, including high material costs, degradation under ambient conditions, instability under UV light, and sensitivity to harsh processing.[1,16–19] Additionally, the fabrication of inorganic ETLs often requires high-temperature treatment, and their optoelectronic properties are challenging to control.[20,21] These limitations collectively hinder the scalability and commercial viability of PSC technologies.

Recently, self-assembled monolayers (SAMs) of tailored molecular species have emerged as cost-effective and versatile alternatives to charge-transporting layers in PSCs. Dipolar small molecules chemically bound to transparent conductive substrates, e.g., indium tin oxide (ITO) or fluorine-doped tin oxide (FTO), can form ultrathin SAMs only a few nanometers thick. These SAMs act as charge-selective contacts by facilitating selective charge extraction through the interfacial electric field induced by their molecular structure and interactions with the adjacent layers.[22] Structurally, SAM molecules typically consist of an anchoring group that facilitates adsorption onto the substrate and a functional group that tailors interfacial properties. A spacer that acts as the backbone bridging the anchoring and functional groups, is also often present and can affect the monolayer self-assembly. By optimizing these functional components of a SAM molecule, the resulting charge-selective layer can be designed to align energy levels, enhance charge extraction efficiency, passivate trap states, and improve the wettability of the perovskite precursor solution.[1,5,23–27] Furthermore, depending on the intrinsic properties of their molecular structure, SAMs can also be engineered to serve as either hole- or electron-selective contacts.

While most research has concentrated on hole-selective SAMs,[28–41] SAMs as electron-selective contacts (ESCs) for n–i–p devices are more recently gaining attention for their ability to passivate defects and align energy levels.[20,42–45] Among these, naphthalimide derivatives stand out as promising electron transport materials due to their high thermal stability and electron mobility.[20,23] Despite the great promise of electron-selective SAMs for n–i–p PSCs, studies on their design and functionality remain limited. A deeper understanding of how functional group modifications influence surface properties and device performance is crucial.

In this report, a series of naphthalimide derivatives was designed, synthesized, and investigated to construct ESCs through a chemical adsorption-based self-assembly method. The molecular design focused on systematically modifying the functional groups to tune the interfacial electronic structure and surface wettability, which are two critical parameters that influence charge extraction and perovskite film formation in PSCs. Functional groups with varied electronic characteristics (ranging from electron-donating to electron-withdrawing) and steric hindrance were incorporated to modulate the energy levels and molecular packing behavior. The structural modifications of the substituents on the naphthalimide unit significantly influenced both the molecular energy levels and surface properties of the self-assembled ESCs. As a result, the power conversion efficiency (PCE) of n-i-p structured PSCs was significantly varied from 5.8% to 20.6%, providing important insights into molecular design rules for SAM molecules.

2. Results and Discussion

With the n–i–p PSC device structure used in this work (**Figure 1a**), the core molecule of 1,8-naphthalimide for the SAM ESC was carefully chosen due to its electron-withdrawing ability, and a phosphonic acid anchoring group along with a solubilizing alkyl chain was employed to link the core naphthalimide moiety to the transparent conductive substrate (e.g., ITO). This base molecular structure (denoted as NI, Figure 1b) served as a control SAM molecule while three different functional groups, electron-withdrawing cyano- (NI-CN), electronegative bromo- (NI-Br), and electron-donating methoxy- (NI-OMe) groups, were introduced as pendant groups onto NI to examine their influence on charge extraction efficiency as ESCs. Moreover, since the energy levels of the NI derivatives were varied depending on the functional pendant groups, a direct comparison amongst these derivatives allowed the identification of key factors governing electron extraction efficiency between the influence of energy levels and the chemical nature of the pendant groups. In addition, the effect of different alkyl chain spacer lengths was probed with the NI-CN structure, e.g., NI-CN-P with a propyl and NI-CN-B with a butyl chain represented longer linkers than the default ethyl chain. The chemical characterization of the prepared molecules (NI, NI-CN, NI-CN-P, NI-CN-B, NI-Br, and NI-OMe) and detailed synthetic routes are provided in the Experimental Section and Supporting Information.

The formation of SAMs involves the self-organization of molecules bonding through the phosphonic acid-anchoring group onto the metal oxide surface. Since the performance of PSCs incorporating charge-selective SAMs is significantly influenced by SAM coverage, the deposition process was optimized individually for each SAM based on the corresponding device performance, aiming to ensure consistent film quality and functionality.[46] Following spin-coating of the SAM solution onto the ITO substrate, various annealing temperatures and rinsing solvents were tested to optimize the anchoring of SAM molecules and to remove any unbound molecules while minimizing potential thermal degradation. To evaluate the impact of the newly developed SAMs as ESCs on photovoltaic (PV) device performance and their potential as substitutes for conventional ETLs in PSCs, we fabricated a series of n-i-p PSCs with only SAMs as the ESC and triple cation perovskites ($Cs_{0.05}(FA_{0.83}MA_{0.17})_{0.95}Pb(I_{0.83}Br_{0.17})_3$) in the configuration ITO/SAM/Perovskite/Spiro/Au. The perovskite films were synthesized using a conventional solution processing method and deposited onto the SAM-based ESC layer through a one-step procedure. Chlorobenzene (CB) was employed as an anti-solvent during this process, following the detailed protocol provided in the Experimental Section.

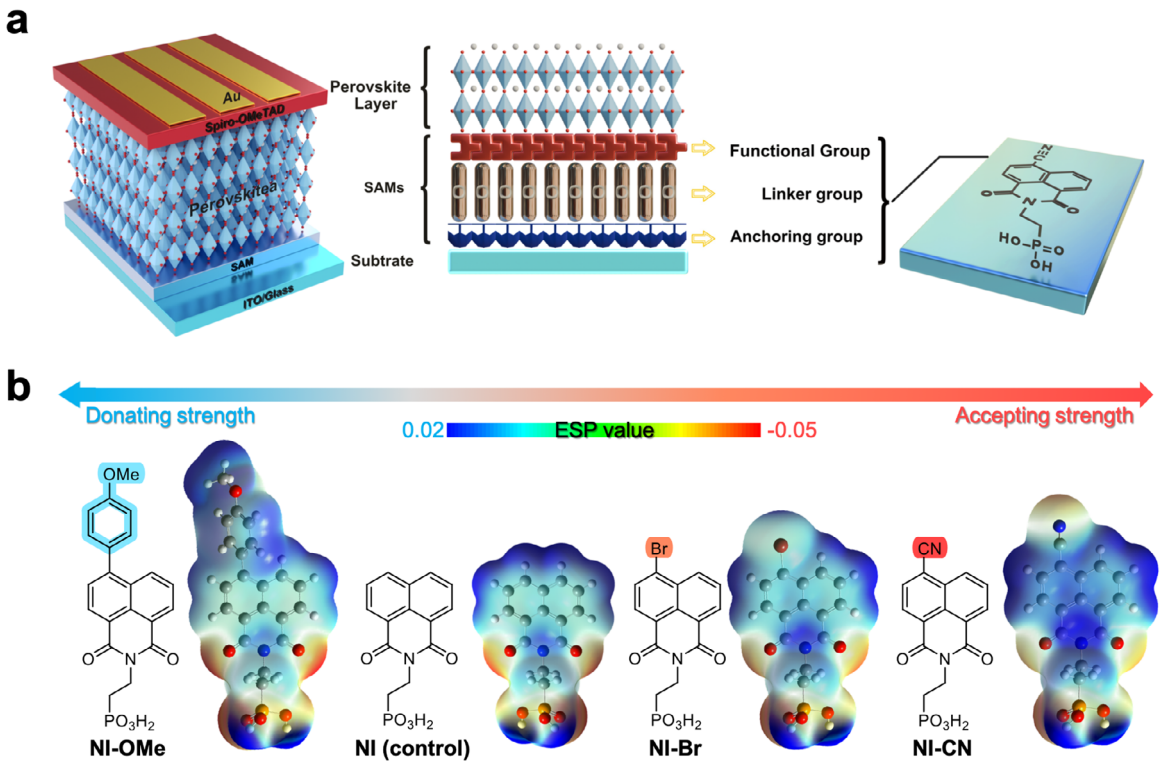

Figure 1. a) Schematic illustration of the PSC configuration used in this work that details the component structure of the SAM molecules, and b) the molecular structures with electrostatic potential values of the SAMs investigated.

For NI, NI-Br, and NI-OMe, pure ethanol (EtOH) was identified as the optimal solvent, and the annealing temperature was optimized to 100 °C. As shown in Figure S1 (Supporting Information), high-temperature annealing (>100 °C) appeared to cause a noticeable reduction in the PV performance of PSCs prepared with NI as a SAM, highlighting the importance of carefully controlled processing conditions. The reason for performance dependence on the annealing temperature is likely ascribed to a change in the substrate surface energy level. As an example, the surface potential of NI changes with the annealing temperature (Figure S2, Supporting Information). The result implies an upward shift of energy level when increasing the annealing temperature from 100 to 140 °C, leading to reduced charge extraction from the perovskite layer to the ITO, which is consistent with the trend in J_{sc} (Figure S1, Supporting Information). The effect of thermal annealing on the molecular stacking has been observed in organic semiconductors (e.g., naphthalene diimide-based materials).[47] Therefore, a change in the dipole effect from an altered packing of the molecules is reasonably expected. In contrast, for NI-CN, a mixed solvent system of EtOH and toluene (1:1, v/v) resulted in improved PV performance, which is attributed to its limited solubility in pure EtOH. The optimized annealing temperatures for NI-CN were 140 °C, as shown by PV performance (Figure S3, Supporting Information). For subsequent experiments, each SAM was processed using optimized protocols, ensuring reproducible and high-quality SAM films. Contact angle measurements verified the successful molecular functionalization of ITO substrates (Figure S4, Supporting Information). A significant change in the angle has been observed for all SAM materials, compared to ITO (Figure S5, Supporting Information), which implies chemical bonding of the molecules with the ITO surface. It is noted that the differences in the angle observed between the SAM materials can be related to the different functional groups in the pendant position. In order to examine the thermal stability of SAM molecules, thermogravimetric analysis (TGA) was employed (Figure S6, Supporting Information). From the TGA curves, a minor mass loss (1–3%) was observed below 100 °C, which is primarily attributed to the loss of adsorbed water. Notably, more than 99.5% of the samples' mass was retained within the temperature range between 100 and 200 °C, indicating that the thermal annealing process does not lead to significant chemical degradation of the SAM molecules.

Under the optimized conditions for each molecule, **Figure 2** depicts the statistical distributions of PV performance parameters acquired under standard AM1.5G 1-sun testing conditions, including PCE, open-circuit voltage (V_{OC}), short-circuit current density (J_{SC}), and fill factor (FF), obtained from multiple different batches of devices. Remarkably, compared to the control molecule, NI, employing NI-CN as the SAM significantly enhanced the PCE of the solar cells, increasing from an average of 3.84 ± 1.58% for NI to 16.98 ± 1.75% for NI-CN. Among the cyano-functionalized SAMs (NI-CN, NI-CN-P, and NI-CN-B), the highest PCE was achieved with the SAM containing an ethyl chain (NI-CN). This suggests that the length of the alkyl chain influences the interaction between the substrate and the perovskite, with shorter chains facilitating charge extraction or electron selection and contributing to better overall device

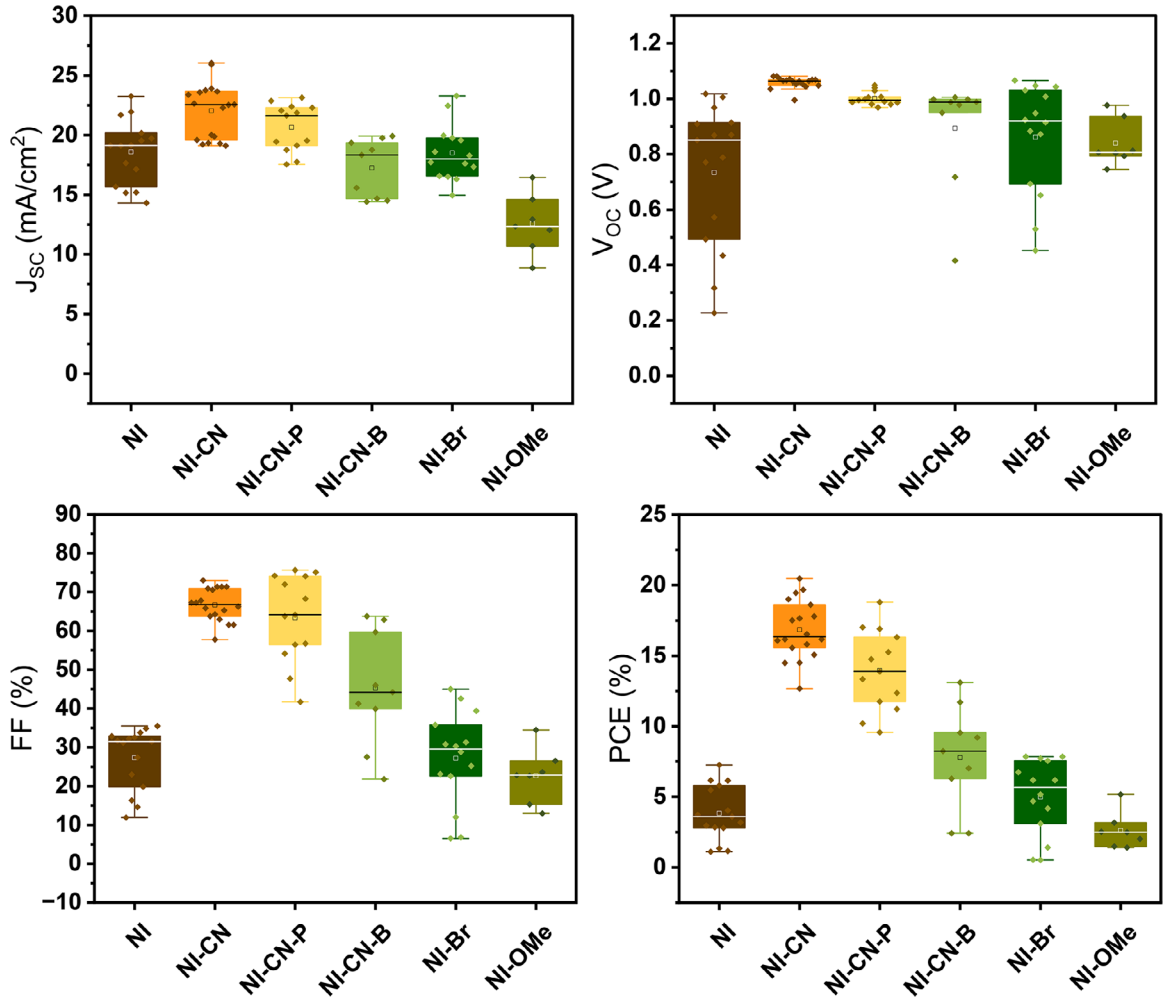

Figure 2. Statistical distribution of photovoltaic performance parameters for the synthesized SAMs-based devices tested at 1-sun (100 mW cm^{-2}), including the short-circuit current density (J_{SC}), open-circuit voltage (V_{OC}), fill factor (FF), and power conversion efficiency (PCE).

performance. Kelvin probe force microscopy (KPFM) measurements (Figure S7, Supporting Information) give more insight into this observation by showing relatively inhomogeneous surface potentials for SAMs with longer alkyl chains despite showing similar topologies. Indeed, the NI-CN-B SAM exhibited a particularly patchy surface potential with domains on the order of 1 µm in dimension, suggesting less uniform and less favorable interfacial properties for efficient charge extraction. Additionally, analysis of the statistical distribution of surface potentials of NI, NI-CN, and NI-CN-B shows similar peak widths for NI and NI-CN; however, for NI-CN-B, the distribution was noticeably broader (Figure S8, Supporting Information). The improved homogeneity in the surface potential of NI and NI-CN is attributed to a more homogeneous molecular alignment and suppressed formation of distinct molecular crystalline domains.[48,49] Moreover, among NI-CN, NI-CN-P, and NI-CN-B, the KPFM results show that NI-CN exhibited the most negative surface potential, which corresponds to a relatively high work function. This is likely due to the strong electron-withdrawing properties of the cyano terminal groups and the relatively shorter length of the molecule. Since a higher work function indicates a deeper interfacial energy level alignment, which facilitates more efficient electron extraction from the perovskite conduction band, this is likely a key factor resulting in the observed improvement in PV performance.

The PV performance of PSCs prepared with the NI-Br molecule as a SAM showed slightly better performance compared to the control NI-based PSCs, but the PCE still remained much lower than that of NI-CN-based PSCs. This suggests that any possible benefit of the pendant halide, and its possible interaction with the perovskite layer, is marginal compared to other factors of the ESC. Meanwhile, the PV performance of NI-OMe was extremely low, with an average efficiency of 2.61 ± 0.89%, suggesting that the electron-donating methoxy functional group severely hinders charge extraction. This poor performance could be attributed to unfavorable energy level alignment leading to a blocked electron extraction at the SAM/perovskite interface, which will be discussed later (vide infra).

Focusing on the difference between the best-performing SAM (NI-CN) and the control structure (NI), representative current density-voltage (J–V) curves for PSCs prepared with these ESCs are shown in **Figure 3a**, with the corresponding PV

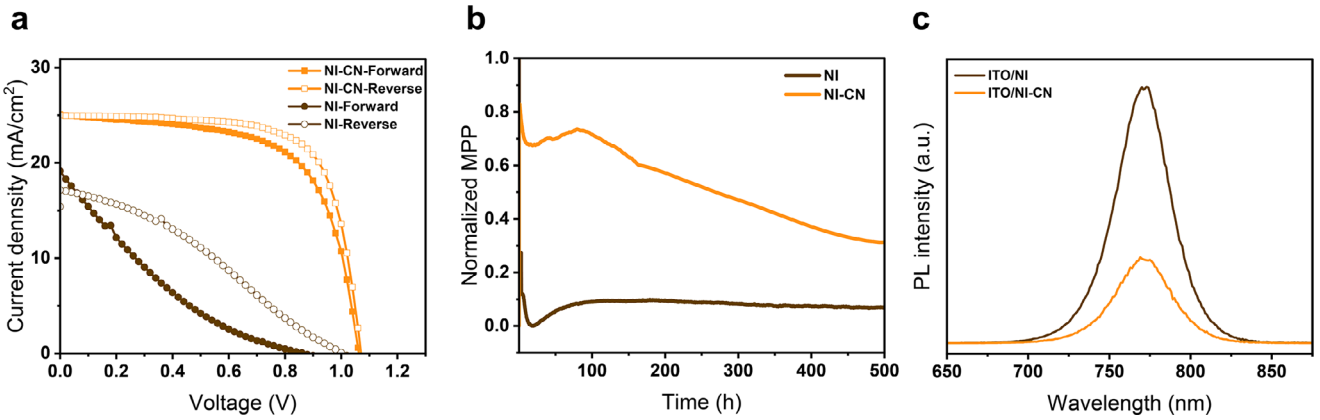

Figure 3. Characterization of synthesized SAM-based devices. a) Current–voltage scans for the best performing device, b) long-term stability of NI, and NI-CN based devices under constant 1-sun illumination without encapsulation, maintaining temperatures between 50 to 60 °C, and c) steady-state PL spectra of ITO/SAM/perovskite samples.

parameters summarized in **Table 1**. We note that the champion cell, attributed to the optimized condition of NI-CN, exhibited an impressive PCE of 20.64%, a high V_{OC} of 1.07 V, a substantial J_{SC} of 25.01 mA cm^{-2}, and a FF of 70.6%. It is worth noting that the PCE with NI-CN is very comparable with the performance achieved with SnO_2-ETL (a PCE of 18.67%, V_{OC} of 1.02 V, J_{SC} of 22.48 mA cm^{-2}, and FF of 74.8% in Figure S9, Supporting Information). In contrast, the control champion cell with NI achieved a PCE of 5.81%, V_{OC} of 1.01 V, J_{SC} of 17.15 mA cm^{-2}, and FF of 32.2% as detailed in Table 1.

Long-term stability tests were performed on PSC devices based on both NI, NI-CN, and SnO_2 (Figure S9, Supporting Information) under continuous 1 sun illumination with maximum power point (MPP) tracking for up to 500 h. The measurements were performed without encapsulation, in air, and using a light-soaking chamber maintained at 50–60 °C. As shown in Figure 3b and Figure S9 (Supporting Information), the NI- and SnO_2-based devices exhibited a significant initial drop in performance during the early hours of MPP tracking. In contrast, the NI-CN-based device demonstrated improved stability, showing only a gradual decline with a smooth slope over the 500-h test period. Given our MPP testing conditions (i.e., unencapsulation devices at 1-sun in ambient atmosphere), the degradation is most likely associated with the degradation of perovskite. Indeed, ^{1}H-NMR was employed to verify the photostability of all SAMs (See Experimental Section, "Synthesis of SAM molecules" for more details). Particularly, the photostability of NI-CN was further verified by contact angle measurement. After 200 h of continuous illumination of a bare SAM film in an N_2 atmosphere, the contact angle increased compared to the initial value (Figure S5, Supporting Information). The reason for the increased value is plausibly owing to the N_2 environment, since the hydrophobicity of a bare ITO also increased slightly under N_2. Therefore, the maintained difference between the bare ITO and NI-CN coated sample after continuous light illumination implies excellent photostability of the NI-CN SAM. This enhanced operational stability may be attributed to the electron-withdrawing nature of the cyano functional group in NI-CN,[50] which can promote stronger interfacial interactions. These features may help suppress interfacial degradation and improve morphological stability under thermal and illumination stress. These results highlight the crucial role of the functional group in enhancing the long-term stability of the devices under harsh environmental conditions.

To further evaluate the effect of electron-selective SAMs, perovskite films prepared with underlying NI or NI-CN SAMs or SnO_2 (as a conventional ETL) were subjected to aggressive thermal stress by heating at 130 °C for 4 h in an N_2 glovebox. The optical properties of the coated perovskite films were examined before and after thermal stress. Analysis of the absorption spectra (Figure S10, Supporting Information) revealed a significant reduction in absorption at shorter wavelengths for the perovskite coated on SnO_2, suggesting degradation in the perovskite film induced by thermal stress. Prior to thermal stress exposure, the surface morphology of perovskite films coated with different SAM layers was analyzed using scanning electron microscopy (SEM), showing no notable differences in morphology (Figure S11, Supporting Information). This underscores the critical role of the SAM layer as an ESC in preserving the perovskite phase under thermal stress. While NI and NI–CN performed similarly, the NI–CN-coated perovskite maintained a smoother and more

Table 1. Photovoltaic parameter data of the NI- and NI-CN-based champion cells.

		J_{SC} [mA cm^{-2}]	V_{OC} [V]	FF [%	PCE [%]
NI	Forward	19.15	0.87	16.30	2.85
	Reverse	17.15	1.01	32.20	5.81
NI-CN	Forward	25.08	1.06	63.8	18.58
	Reverse	25.01	1.07	70.6	20.64

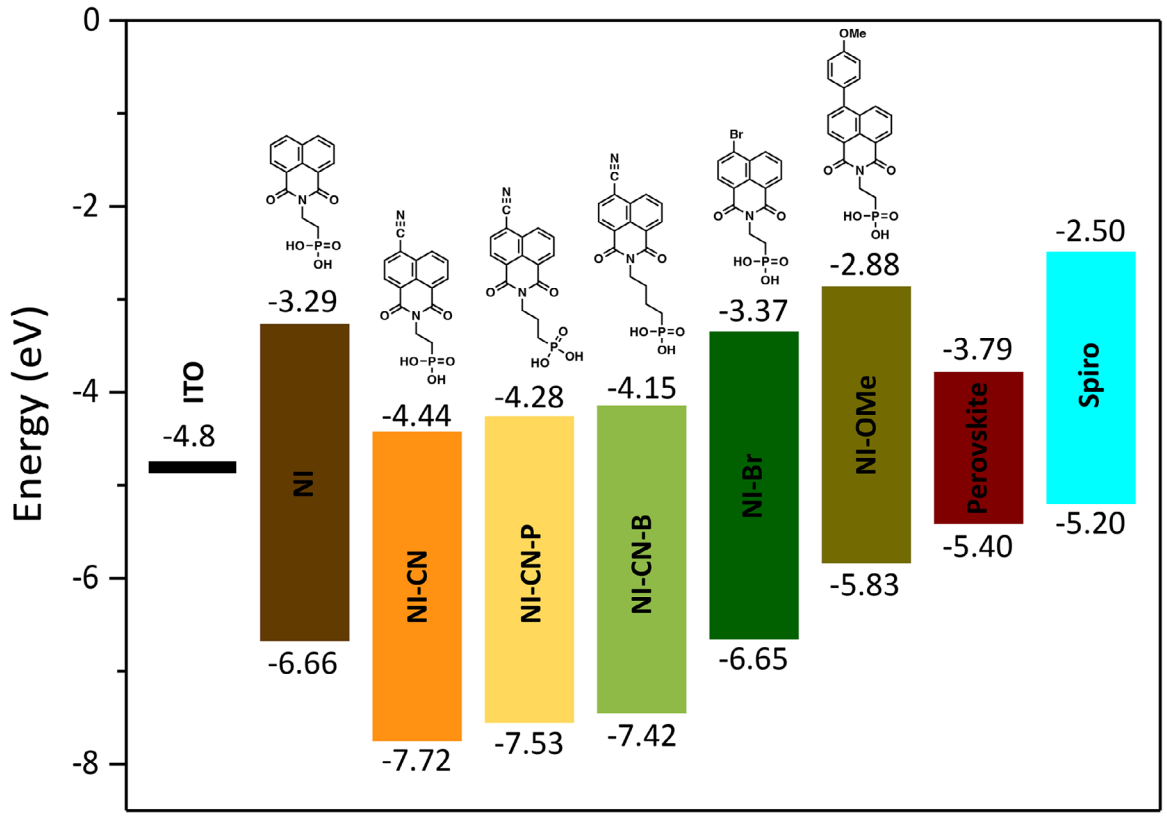

Figure 4. Estimated energy level diagram of SAM-modified ITO electrodes, derived from UPS measurement and UV–vis spectroscopy. It is noted that the energy levels of the perovskite and spiro-OMeTAD reported in the ref. [51,52] are used.

stable absorbance spectrum at shorter wavelengths, confirming its relatively superior thermal stability.

Photoluminescence (PL) spectroscopy of thin films with the ITO/SAM/Perovskite architecture gave further insight into the performance difference between these SAMs by comparing the control SAM (NI) to the best-performing SAM (NI-CN). As shown in the PL spectra (Figure 3c), the sample containing NI exhibits higher PL intensity compared to that of the NI-CN-based device. The reduced PL intensity observed for the samples containing NI-CN indicates more efficient PL quenching, likely due to improved charge extraction at the interface, which competes with non-radiative and/or radiative recombination, thereby reducing the PL emission.

In order to further elucidate the PV performance difference when employing the different SAMs, the alignment of energy levels between SAM-functionalized ITO and the active layer was estimated using ultraviolet photoelectron spectroscopy (UPS) and UV–vis. The schematic in **Figure 4** illustrates the estimated energy levels. Detailed UPS spectra of the SAM-functionalized ITO, including secondary electron cutoff and onset regions, are provided in Figure S12 (Supporting Information). The energy of the highest occupied molecular orbital (E_{HOMO}) of each SAM on the ITO was calculated using the equation $E_{HOMO} = -[21.22\ eV - (E_{cutoff} - E_{onset})]$, where E_{cutoff} is the higher binding energy cutoff, and E_{onset} is the onset energy in the HOMO.[51] To determine the energy of the lowest unoccupied molecular orbital (E_{LUMO}) of the SAM films, the HOMO-LUMO gap energy was determined optically using the onset absorption edge from UV–vis spectra (Figure S12, Supporting Information). In addition, to corroborate the experimental results shown in Figure 4, density-functional theory (DFT) simulation of the energy levels was performed using Gaussian 09 with the B3LYP/6-31G(d) hybrid density functional/basis set combination. Variation in the functional groups on the naphthalimide resulted in significant differences in the calculated energy levels (as shown in Figure S13, Supporting Information) with a similar trend to that shown in Figure 4, despite a slight difference in the absolute value of the calculated energy levels. In both the experimental case (−4.4 eV vs vacuum) and the DFT simulations (−3.15 eV vs vacuum), the NI-CN showed the deepest E_{LUMO}.

Compared with the work function (WF) of bare ITO (−4.8 eV),[53] the deposition of the electron-selective SAMs on ITO led to a raised (closer to vacuum) energy level for electron transport (E_{LUMO}). The most notable shift was observed for the experimental results of NI-OMe, which reached −2.88 eV, attributed to its electron-donating methoxy group. This extremely high E_{LUMO} suggests the SAM acts as a barrier for charge extraction from the perovskite layer to the ITO, given the reported energy levels for the perovskite.[51,52] This barrier hinders electron transfer from the perovskite conduction band to the ITO, except in cases where tunneling mechanisms[54] can overcome this barrier. This explains the poor performance of the NI-OMe and NI-Br SAMs.

In stark contrast, the well aligned E_{LUMO} of the SAMs containing the CN group between the conduction band level of the

perovskite layer and the WF of the ITO, can facilitate efficient electron injection from the perovskite conduction band to the LUMO level of the SAM with less potential losses, which can explain the enhanced photovoltaic performance observed with these SAMs. Indeed, as a strong electron-withdrawing group, the CN group delocalizes the electron density toward the C≡N moiety, as suggested by the DFT results, resulting in a significant reduction in the energy levels compared to the other SAMs. Although NI-CN derivatives with longer alkyl chains (propyl and butyl) were introduced, the stronger electron-donating character of the alkyl groups compared to ethyl led to a less favorable shift of E_{LUMO}, which, in addition to the electrically insulating nature of the alkyl chain and the aforementioned inhomogeneity of the surface, contributes to their poorer performance compared to NI-CN. Overall, the alignment of the energy levels in addition to favorable surface homogeneity and a short linker appear to be the most important design considerations for SAM-based ESCs for n-i-p PSCs. It is noted that no obvious difference was detected by XRD analysis (Figure S14, Supporting Information). However, other factors, including possible chemical interaction to improve SAM/perovskite interfacial properties (e.g., reduced defect density),[50] suggest that further study on the interface will be required to fully elucidate the dominant effect.

3. Conclusion

This study presents a systematic investigation into the molecular engineering of self-assembled monolayer electron-selective contacts using novel NI derivatives with various functional groups for n–i–p perovskite solar cells. The results reveal that the nature of the functional group significantly influences interfacial properties, film formation, and overall device performance. Among the investigated SAMs, the control NI molecule, and its -Br and -OMe functionalized analogues, all showed very poor performance, which was attributed to a poor alignment of the SAM E_{LUMO} with the perovskite conduction band. The cyano-functionalized derivative (NI-CN) demonstrated superior performance, achieving a champion PCE of 20.64%. This enhancement is attributed to improved energy level alignment, efficient charge extraction, and reduced interfacial recombination, as supported by UPS, PL quenching, and *J–V* measurements. Although electron-selective SAMs have been seldom reported as standalone interlayers without relying on metal oxide ETLs, the performance achieved in this work notably represents one of the highest PCE, exceeding 20%, among PSCs employing standalone electron-selective SAMs (See Table S2, Supporting Information for relevant references). Moreover, for the cyano-functionalized derivative (NI-CN), varying length of alkyl chain and the corresponding energetic inhomogeneity of the SAM functionalized ITO surface were found to contribute to the poorer performance of NI-CN-P and NI-CN-B compared to NI-CN and suggested important design considerations for SAM-based ESCs. Overall, these findings highlight the potential of functionalized SAMs as low-cost, tunable, and efficient electron-selective materials, offering a scalable and versatile alternative to conventional inorganic contacts for the scalable production of high-performance, commercially practical PSCs.

4. Experimental Section

Materials: All materials used in this study were commercially available (except the SAM molecules, which were synthesized for this study), and all solvents and chemicals were used without further purification.

Methods—Synthesis of SAM Molecules: Detailed synthetic procedures are given in the Supporting Information. Nuclear magnetic resonance (NMR), high-resolution matrix-assisted laser desorption ionization time-of-flight (MALDI-TOF), and elemental analysis confirmed their structures and are shown in Figures S15–S26 and Table S1 (Supporting Information). To assess the photostability of all SAM molecules, ^{1}H-NMR analysis was employed after exposing SAM molecule solutions to continuous illumination. No new peaks or changes in chemical shifts of the aromatic and aliphatic protons (in DMSO-d_6) were observed for all SAM molecules after light exposure (AM1.5G, 100 mW cm^{-2} for 24 h), see Figure S27 (Supporting Information).

Methods—Perovskite Precursor Solutions: The perovskite active layers were deposited from a precursor solution containing CsI, FAI, PbI_2, MABr, and $PbBr_2$ in anhydrous DMF:DMSO (4:1 v/v) in amounts according to the following formula of a triple cation perovskite: $Cs_{0.05}(FA_{0.83}MA_{0.17})_{0.95}Pb(I_{0.83}Br_{0.17})_3$.

Methods—Solar Cell Device Fabrication: Patterned indium-doped tin oxide (ITO) coated glass substrates (20 mm × 25 mm) were cleaned sequentially with 2% Hellmanex aqueous solution, acetone, and isopropanol under ultrasonication for 30 min, respectively. Substrates were dried with N_2 blowing and then treated with UV-ozone for 15 min.

Regular n–i–p architecture PSCs were fabricated (Figure 1). The SAM functionalization was performed using solutions with concentrations of 1 mM in absolute ethanol or EtOH:Toluene (1:1 v/v). Solutions (100 µL) were spin-coated on the ITO substrates at a speed of 3000 rpm for 30 s, followed by annealing at 100 and 140 °C for 10 min. Following annealing, the substrates were rinsed with the same solvent used for coating, using the same spin-coating parameters as during the initial deposition. Subsequently, 80 µL perovskite precursor solution was spin-coated on the ITO/SAM layer at 6000 rpm for 30 s with a ramp of 2000 rpm s^{-1}. About 17 s prior to the end of the program, 200 µL chlorobenzene as an anti-solvent was dripped onto the pre-perovskite film. Then the substrates were quickly transferred to a hot plate for 60 min at 100 °C. It was noted that all perovskite and SAM deposition procedures were performed in N_2 atmospheric glove box conditions.

Then, a 2,2,7,7′-tetrakis-(N,N-di-4-methoxyphenylamino)-9,9′-spirobifluorene (Spiro-OMeTAD, Lumtec) solution (70 mM in chlorobenzene) was spin-casted at 4000 rpm for 20 s. Spiro-OMeTAD was doped with Li-TFSI and 4-tert-butylpyridine (TBP, Sigma–Aldrich). The molar ratio of the spiro-OMeTAD additives to spiro was 0.5 and 3.3 for Li-TFSI and TBP, respectively. Finally, 80 nm of gold was thermally evaporated under high vacuum as the top electrode.

Characterization: Photovoltaic devices were measured using a source meter (Keithley 2400) under simulated AM 1.5 illumination (100 mW cm^{-2}) provided by a xenon arc lamp filtered by a KG-2 filter (Schott glass). The light source intensity was adjusted using the spectral mismatch method and calibrated using a standard Si solar cell. The active area defined by a metal mask aperture was 0.09 cm^2. Operational stability was measured by the maximum power point tracking (MPPT) method under 1 sun illumination at ambient conditions.

UV–vis measurements were performed with a UV-3600 (Shimadzu) using a 60 mm integrating sphere. The samples were measured using ITO as a baseline correction according to the substrates.

Photoluminescence measurements were performed on perovskite films deposited on ITO/SAM substrates using a Fluorolog-3 modular spectrofluorometer (Horiba) with an excitation light of 600 nm and 8 nm bandpass.

Scanning electron microscopy images were carried out with SEM (Zeiss Merlin In-Lens detectors).

Ultraviolet photoelectron spectroscopy was conducted on ITO/SAM substrates with an Axis Supra (Kratos Analytical) using 21.22 eV photons

emitted by a He I UV source. The pass energy was set to 10 eV with a step size of 0.025 eV. The samples were electrically grounded to limit charging effects.

Atomic force microscopy (AFM) and Kelvin probe force microscopy (KPFM) were measured with a Cypher S (Asylum Research), equipped with a Pt-coated cantilever (Olympus AC240TM).

Contact angle measurements were performed at room temperature by using a Kruss drop shape analyzer (DSA25S) and analyzed by the Kruss Advance software through the sessile drop method. The water droplet volume was kept at 2 µL.

Supporting Information

Supporting Information is available from the Wiley Online Library or from the author.

Acknowledgements

The authors thank the EPFL and the research agreement between EPFL and the Korea Electric Power Corporation (KEPCO) for financial support of this work. This work was also supported by the National Research Foundation of Korea (NRF) grant funded by the Korea government (Ministry of Science and ICT, MSIT) (No. RS-2023-00211341 and No. RS-2023-00217968). Additionally, the authors appreciate the contributions of Dr. Mounir Mensi from EPFL for conducting UPS measurements.

Open access publishing facilitated by Ecole polytechnique federale de Lausanne, as part of the Wiley - Ecole polytechnique federale de Lausanne agreement via the Consortium Of Swiss Academic Libraries.

Conflict of Interest

The authors declare no conflict of interest.

Data Availability Statement

The data that support the findings of this study are available from the corresponding author upon reasonable request.

Keywords

electron selective materials, halide perovskite solar cells, self-assembled monolayers

Received: May 21, 2025
Revised: August 18, 2025
Published online:

[1] W. Li, E. Martínez-Ferrero, E. Palomares, *Mater. Chem. Front.* **2024**, *8*, 681.
[2] https://www.nrel.gov/pv/cell-efficiency.html (accessed: August 2025).
[3] P. Ferdowsi, S.-J. Kim, T.-D. Nguyen, J.-Y. Seo, J.-H. Yum, K. Sivula, *J. Mater. Chem. A* **2024**, *12*, 15837.
[4] M. A. Ruiz-Preciado, D. J. Kubicki, A. Hofstetter, L. McGovern, M. H. Futscher, A. Ummadisingu, R. Gershoni-Poranne, S. M. Zakeeruddin, B. Ehrler, L. Emsley, J. V. Milić, M. Grätzel, *J. Am. Chem. Soc.* **2020**, *142*, 1645.
[5] C. E. P. Galvis, D. A. G. Ruiz, E. Martínez-Ferrero, E. Palomares, *Chem. Sci.* **2024**, *15*, 1534.
[6] J. Suo, B. Yang, D. Bogachuk, G. Boschloo, A. Hagfeldt, *Adv. Energy Mater.* **2024**, *15*, 2400205.
[7] M. Saliba, T. Matsui, J.-Y. Seo, K. Domanski, J.-P. Correa-Baena, M. K. Nazeeruddin, S. M. Zakeeruddin, W. Tress, A. Abate, A. Hagfeldt, M. Grätzel, *Energy Environ. Sci.* **2016**, *9*, 1989.
[8] P. Ferdowsi, E. Ochoa-Martinez, U. Steiner, M. Saliba, *Chem. Mater.* **2021**, *33*, 3971.
[9] L. Xie, J. Chen, P. Vashishtha, X. Zhao, G. S. Shin, S. G. Mhaisalkar, N.-G. Park, *ACS Energy Lett.* **2019**, *4*, 2192.
[10] S. Jeong, J. Oh, J. Park, Y. Cho, S. Jung, S. Lee, J. Park, C. Yang, *ACS Energy Lett.* **2024**, *9*, 3771.
[11] R. Sorrentino, E. Kozma, S. Luzzati, R. Po, *Energy Environ. Sci.* **2021**, *14*, 180.
[12] N. Ahmad, H. Zhou, P. Fan, G. Liang, *EcoMat* **2022**, *4*, 12156.
[13] H. Min, D. Y. Lee, J. Kim, G. Kim, K. S. Lee, J. Kim, M. J. Paik, Y. K. Kim, K. S. Kim, M. G. Kim, T. J. Shin, S. Il Seok, *Nature* **2021**, *598*, 444.
[14] J. Park, J. Kim, H.-S. Yun, M. J. Paik, E. Noh, H. J. Mun, M. G. Kim, T. J. Shin, S. I. Seok, *Nature* **2023**, *616*, 724.
[15] Y. Zhao, F. Ma, Z. Qu, S. Yu, T. Shen, H.-X. Deng, X. Chu, X. Peng, Y. Yuan, X. Zhang, J. You, *Science* **2022**, *377*, 531.
[16] Z. Zhu, K. Mao, K. Zhang, W. Peng, J. Zhang, H. Meng, S. Cheng, T. Li, H. Lin, Q. Chen, X. Wu, J. Xu, *Joule* **2022**, *6*, 2849.
[17] M. Degani, Q. An, M. Albaladejo-Siguan, Y. J. Hofstetter, C. Cho, F. Paulus, G. Grancini, Y. Vaynzof, *Sci. Adv.* **2021**, *7*, abj7930.
[18] S. Chen, X. Dai, S. Xu, H. Jiao, L. Zhao, J. Huang, *Science* **2021**, *373*, 902.
[19] Z. Li, B. Li, X. Wu, S. A. Sheppard, S. Zhang, D. Gao, N. J. Long, Z. Zhu, *Science* **2022**, *376*, 416.
[20] L. Li, Y. Wu, E. Li, C. Shen, H. Zhang, X. Xu, G. Wu, M. Cai, W.-H. Zhu, *Chem. Commun.* **2019**, *55*, 13239.
[21] M. F. M. Noh, C. H. Teh, R. Daik, E. L. Lim, C. C. Yap, M. A. Ibrahim, N. A. Ludin, A. R. bin, M. Yusoff, J. Jang, M. A. M. Teridi, *J. Mater. Chem. C* **2018**, *6*, 6038.
[22] Q. Wang, C.-C. Chueh, T. Zhao, J. Cheng, M. Eslamian, W. C. H. Choy, A. K.-Y. Jen, *ChemSusChem* **2017**, *10*, 3794.
[23] H. Cheng, Y. Li, Y. Zhong, *Mater. Chem. Front.* **2023**, *7*, 3958.
[24] S. A. Paniagua, A. J. Giordano, O. L. Smith, S. Barlow, H. Li, N. R. Armstrong, J. E. Pemberton, J.-L. Brédas, D. Ginger, S. R. Marder, *Chem. Rev.* **2016**, *116*, 7117.
[25] P. J. Hotchkiss, S. C. Jones, S. A. Paniagua, A. Sharma, B. Kippelen, N. R. Armstrong, S. R. Marder, *Acc. Chem. Res.* **2012**, *45*, 337.
[26] T. Zhu, J. Su, F. Labat, I. Ciofini, T. Pauporté, *ACS Appl. Mater. Interfaces* **2020**, *12*, 744.
[27] F. Ali, C. Roldán-Carmona, M. Sohail, M. K. Nazeeruddin, *Adv. Energy Mater.* **2020**, *10*, 2002989.
[28] M. Li, Y. Xie, F. R. Lin, Z. Li, S. Yang, A. K.-Y. Jen, *The Innovation* **2023**, *4*, 100369.
[29] A. Magomedov, A. Al-Ashouri, E. Kasparavičius, S. Strazdaite, G. Niaura, M. Jošt, T. Malinauskas, S. Albrecht, V. Getautis, *Adv. Energy Mater.* **2018**, *8*, 1801892.
[30] A. Al-Ashouri, A. Magomedov, M. Roß, M. Jošt, M. Talaikis, G. Chistiakova, T. Bertram, J. A. Márquez, E. Köhnen, E. Kasparavičius, S. Levcenco, L. Gil-Escrig, C. J. Hages, R. Schlatmann, B. Rech, T. Malinauskas, T. Unold, C. A. Kaufmann, L. Korte, G. Niaura, V. Getautis, S. Albrecht, *Energy Environ. Sci.* **2019**, *12*, 3356.
[31] A. Farag, T. Feeney, I. M. Hossain, F. Schackmar, P. Fassl, K. Küster, R. Bäuerle, M. A. Ruiz-Preciado, M. Hentschel, D. B. Ritzer, A. Diercks, Y. Li, B. A. Nejand, F. Laufer, R. Singh, U. Starke, U. W. Paetzold, *Adv. Energy Mater.* **2023**, *13*, 2203982.
[32] A. Ullah, K. H. Park, Y. Lee, S. Park, A. B. Faheem, H. D. Nguyen, Y. Siddique, K.-K. Lee, Y. Jo, C.-H. Han, S. Ahn, I. Jeong, S. Cho, B. Kim, Y. S. Park, S. Hong, *Adv. Funct. Mater.* **2022**, *32*, 2208793.
[33] E. Arkan, E. Yalcin, M. Unal, M. Z. Y. Arkan, M. Can, C. Tozlu, S. Demic, *Mater. Chem. Phys.* **2020**, *254*, 123435.

[34] E. Arkan, M. Unal, E. Yalcin, M. Z. Yigit Arkan, S. Yurtdas, M. Can, C. Tozlu, S. Demic, *Mater. Sci. Semicond. Process.* **2021**, *123*, 105514.
[35] E. Arkan, M. Z. Yigit Arkan, M. Unal, E. Yalcin, H. Aydin, C. Celebi, M. Can, C. Tozlu, S. Demic, *Opt. Mater.* **2020**, *105*, 109910.
[36] E. Aktas, N. Phung, H. Köbler, D. A. González, M. Méndez, I. Kafedjiska, S.-H. Turren-Cruz, R. Wenisch, I. Lauermann, A. Abate, E. Palomares, *Energy Environ. Sci.* **2021**, *14*, 3976.
[37] Y. Wang, Q. Liao, J. Chen, W. Huang, X. Zhuang, Y. Tang, B. Li, X. Yao, X. Feng, X. Zhang, M. Su, Z. He, T. J. Marks, A. Facchetti, X. Guo, *J. Am. Chem. Soc.* **2020**, *142*, 16632.
[38] Q. Liao, Y. Wang, Z. Zhang, K. Yang, Y. Shi, K. Feng, B. Li, J. Huang, P. Gao, X. Guo, *J. Energy Chem.* **2022**, *68*, 87.
[39] S. Huang, Z. Liu, J. Xu, D. Zhang, H. Dong, Z. Wu, L. Duan, *Chem. Eng. J.* **2022**, *430*, 132986.
[40] J. Cao, C.-K. Liu, V. Piradi, H.-L. Loi, T. Wang, H. Cheng, X. Zhu, F. Yan, *ACS Energy Lett.* **2022**, *7*, 3362.
[41] C.-Y. Chang, H.-H. Huang, H. Tsai, S.-L. Lin, P.-H. Liu, W. Chen, F.-C. Hsu, W. Nie, Y.-F. Chen, L. Wang, *Adv. Sci.* **2021**, *8*, 2002718.
[42] P. Topolovsek, F. Lamberti, T. Gatti, A. Cito, J. M. Ball, E. Menna, C. Gadermaier, A. Petrozza, *J. Mater. Chem. A* **2017**, *5*, 11882.
[43] H. Cheng, Y. Li, M. Zhang, K. Zhao, Z.-S. Wang, *ChemSusChem* **2020**, *13*, 2779.
[44] F. Ye, D. Zhang, X. Xu, H. Guo, S. Liu, S. Zhang, Y. Wu, W.-H. Zhu, *Sol. RRL* **2021**, *5*, 2000736.
[45] S. O. Fürer, K. J. Rietwyk, F. Pulvirenti, D. P. McMeekin, M. A. Surmiak, S. R. Raga, W. Mao, X. Lin, Y. Hora, J. Wang, Y. Shi, S. Barlow, D. S. Ginger, S. R. Marder, U. Bach, *ACS Appl. Energy Mater.* **2023**, *6*, 667.
[46] M. Liu, L. Bi, W. Jiang, Z. Zeng, S.-W. Tsang, F. R. Lin, A. K.-Y. Jen, *Adv. Mater.* **2023**, *35*, 2304415.
[47] T. C. Hidalgo Castillo, W. Shan, G. Ma, H. Zhao, Y. Wang, V. Druet, A. Saleh, X. Gu, S. Inal, *Adv. Mater.* **2025**, *37*, 2411214.
[48] S. Yuan, C. Ge, T. Zhang, G. Su, Q. Qiu, G. Ren, L. Ke, G. Du, G. Zou, N. Zhang, H. Liu, Q. Li, T. Jia, Y.-P. Cai, S. Liu, H.-L. Yip, *J. Am. Chem. Soc.* **2025**, *147*, 24662.
[49] J. Zhou, Y. Luo, R. Li, L. Tian, K. Zhao, J. Shen, D. Jin, Z. Peng, L. Yao, L. Zhang, Q. Liu, S. Zhang, L. Jin, S. Chu, S. Wang, Y. Tian, J. Xu, X. Zhang, P. Shi, X. Wang, W. Fan, X. Sun, J. Sun, L.-Z. Chen, G. Wu, W. Shi, H.-F. Wang, T. Deng, R. Wang, D. Yang, et al., *Nat. Chem.* **2025**, *17*, 564.
[50] L. Liang, Q. Xiong, Z. Zhang, Y. Yu, P. Gao, *Electrochim. Acta* **2022**, *413*, 140172.
[51] M. Thambidurai, S. Foo, K. M. M. Salim, P. C. Harikesh, A. Bruno, N. F. Jamaludin, S. Lie, N. Mathews, C. Dang, *J. Mater. Chem. C* **2019**, *7*, 5028.
[52] J. Song, E. Zheng, L. Liu, X.-F. Wang, G. Chen, W. Tian, T. Miyasaka, *ChemSusChem* **2016**, *9*, 2640.
[53] G. M. K. V., J. George, M. Balachandran, *Emergent Mater.* **2024**, *7*, 17.
[54] C. S. S. Sangeeth, A. Wan, C. A. Nijhuis, *J. Am. Chem. Soc.* **2014**, *136*, 11134.